Journal of Applied Fluid Mechanics, Vol. 18, No. 2, pp. 332-347, 2025.
Available online at www.jafmonline.net, ISSN 1735-3572, EISSN 1735-3645.
https://doi.org/10.47176/jafm.18.2.2629

3-D Numerical Study of Cavitation Evolution Through A Butterfly Valve Model at Different Regulating Conditions

G. Zhang[1], X. Wu[1], Z. Y. Wu[1], H. T. Zhang[1], H. D. Kim[2] and Z. Lin[1†]

[1] *Zhejiang Key Laboratory of Multiflow and Fluid Machinery, Zhejiang Sci-Tech University, Hangzhou, 310018, China*
[2] *Department of Mechanical Engineering, Andong National University, Ando, Republic of Korea*

†Corresponding Author Email: *linzhe0122@zstu.edu.cn*

ABSTRACT

Butterfly valves are critical control equipment widely used in transmission systems across various fields, including energy, water conservancy, materials and chemical industries, metallurgy, and aerospace engineering. Cavitation, induced when the local pressure is decreased to saturated vaporization pressure, is a common phenomenon in butterfly valves and causes severe damage to valve components. Numerical studies were conducted to explore the progression of dynamic cavitation in a butterfly valve under different actual conditions by using Large Eddy Simulation (LES) coupled with Schnerr-Sauer cavitation model. The detailed evolution process of generation, development, and collapse was discussed by analyzing the corresponding vapor volume fraction. With the increase of valve opening, there is a corresponding increase in cavitation volume, leading to the rise of disturbance coefficient in full flow field as well as the decrease of shedding frequency of cavitation. The decline of shedding frequency of cavitation exhibits a sudden and pronounced drop at valve opening degree of 60%, which can be attributed to a shift in cavitation shedding behavior from unilateral to bilateral shedding. Periodic changes in cavitation evolution and the presence of attached cavitation on the upper surface of valve plate are obtained and discussed in detail. A comparative analysis of vortex distribution and structure within the flow field reveals insights into the spatial and temporal correlation between cavitation and vortices. The present study of the cavitation mechanism and the in-depth exploration of the evolution law of cavitation provide a clearer understanding of cavitation phenomenon, offering a reference for the structural optimization of butterfly valve in cavitation inhibition.

Article History

Received March 5, 2024
Revised August 1, 2024
Accepted August 29, 2024
Available online December 4, 2024

Keywords:

Butterfly valve
Cavitation
Periodic evolution
Attached cavitation
Vortex structure

1. INTRODUCTION

The butterfly valve is essential for ensuring safe and consistent system operation. Serving as a regulatory component, it regulates flow and controls valves' opening and closing (Tao et al., 2021) and finds applications in aerospace, energy, petrochemical, biomedical, and many other fields. This valve plays a crucial role in effectively operating fluid transport within pipelines and internal circulation, becoming an integral part of system operations. Moreover, during the design and utilization of the butterfly valve, considering the problem of cavitation occurring within the valve is crucial.

Cavitation refers to the process in which a liquid transforms into a gas when the local pressure falls below its saturation vapor pressure (Yuan et al., 2022). This phenomenon can occur in hydraulic machinery, including valves, pumps, turbines, ship propellers, and hydrofoils. Cavitation represents a significant barrier to improving the energy efficiency of hydraulic machinery. In the initial stages of cavitation, decreases in pump head, turbine output, and efficiency can result in unnecessary energy losses. In addition, cavitation can lead to erosion damage of flowing parts, substantially shortening the maintenance cycle and service life. In severe cases, rotating parts can break, leading to water hammer phenomena and other major accidents. Cavitation has the potential to damage structural components of fluid machinery and can lead to hydraulic vibrations and noise, ultimately resulting in broader destruction and economic implications.

Numerous researchers have conducted extensive studies to mitigate the adverse consequences of cavitation. Feng et al. (2023) performed comprehensive numerical simulations, employing full-wetting techniques, to explore the impact of gap width on tip leakage cavitation. Their findings indicated a gradual decrease in the cavitation inception number as the gap widened. Yang et al. (2023) conducted experiments in a cavitation tunnel for investigating the cavitation flow around heated hydrofoils,

NOMENCLATURE

α	valve opening	μ	dynamic viscosity
μ_t	turbulent vortex viscosity	ξ	disturbance coefficient
ρ	fluid density	σ	surface tension
σ_c	cavitation number	τ_{ij}	viscous stress tensor
B_o	boiling number of the liquid phase	C_d	drag coefficient
g	acceleration of gravity	i	different dimensions of the fluid movement in three-dimensional space, i=1,2,3.
Ja_{sub}	dimensionless constant of liquid subcooling	Kv	flow coefficient
p	fluid pressure	ΔP	pressure drop
Q	flow rate	R_B	bubble radius
t	time	u	velocity
V_b	vapor volume fraction		

identifying attached sheet cavitation and supercavitation occurrences on both heated and unheated hydrofoils. Wang et al. (2022) examined the energy efficiency and noise profiles of NACA0009 hydrofoils, varying the size of the tip clearance.

Xue et al. (2019) investigated cavitation within a nozzle, a common geometric model for cavitation studies. Initially, their research explored how fluctuations in inlet pressure affected cavitation in a liquid nitrogen. They found that while pressure fluctuations frequency can suppress cavitation, the amplitude can increase its severity. They also studied the influence of geometric shape by considering factors such as the inlet edge angle, the radius of the inlet edge angle. These factors significantly influenced cavitation, while the swirl blade had little effect on flow characteristics within the nozzle. In addition, the researchers examined how the outlet diameter, pressure differential, and inlet temperature impacted cavitation at low temperatures in various nozzle designs. The study also provides insights into the correlation between the flow coefficient and pressure swirls temperature and simple convergent nozzles.

The venturi tube, another typical geometric cavitation model, has also been studied. Wang et al. (2020) modifying a prediction formula for pressure fluctuations in cavitation within a venturi tube. The formula can effectively predict hydrofoil cavitation and apply to pressure pulsation in venturi tubes. Kozák et al. (2018) examined the occurrence of cavitation under different flow rates, cavitation numbers in venturi tubes, and with or without a vortex generator. They also explored the relationship between cavitation number and hydraulic loss, the corrected hydraulic loss coefficient, and the vibration acceleration of the tube wall, discovering that the cavitation boundary is not distinct when a vortex generator is present.

Many scholars have considered additional factors, such as modifying the turbulence model, adjusting constants in the cavitation model, or introducing new source terms to simulate cavitation flow. Ye et al. (2020) investigated cavitation flow around a hydrofoil applying a modified model that accounts for surface curvature. Upon examining the vorticity transport equation, they found vortices expansion and the moment term associated with oblique pressure within the vortices significantly are instrumental in the generation and development of cavitation vortices. These cavitation vortices shedding results in pressure fluctuations on the hydrofoil surface. They also observed that the frequency of turbulence pulsation and cavitation vortex development coincide. Sun & Tan (2020) employed a modified cavitation model based on cavitation radius to explore the interaction between cavitation, vortices, and pressure fluctuations within a centrifugal pump. They established a relationship between the frequency of cavitation development and pump rotation frequency. Le et al. (2019a) assessed how altering the cavitation phase change constant impacts the cavitation model and adjusted the size of the heat source in the governing equation to minimize heat input. This adjustment was necessary because heat is converted into the liquid's enthalpy during condensation, leading to overestimating energy input and disregarding energy loss. Le et al. (2019b) also evaluated the accuracy of the modified Merkle cavitation model by comparing it with experimental results and analyzed the influence of the condensation empirical constant in the source term on the cavitation model.

In fluid machinery, extensive analyses have also been conducted regarding the cavitation phenomenon. Yu et al. (2020) looked into the connection between turbine flow instability and cavitation mechanisms under non-standard conditions and compared two pressure fluctuations caused by cavitation: spiral vortex and cavitation volume fluctuation. Li & Yu (2021) examined the cavitation phenomenon of a valve seat in the Rankine cycle of a diaphragm pump and identified two distinct types of internal cavitation: expansion and flow-induced cavitation. As the Reynolds number changes during crank rotation, it becomes necessary to adjust the cavitation model constant accordingly. The thermodynamic effect is considered regarding how thermal constants vary with temperature. Kolovos et al. (2021) studied the effects of inlet pressure and density on cavitation under different lift conditions, considering compressibility in needle valves. Habibnejad et al. (2022) how cavitation in globe valves is affected by factors such as opening degree, inlet velocity, and holes orientation. They discovered that the downward sleeve has the most significant inhibitory effect on cavitation by implementing four different sleeve configurations in the valve: no sleeve, radial sleeve, upward sleeve, and downward sleeve. Li et al. (2020) noted that the most effective method to mitigate cavitation in a globe valve is by increasing the outlet pressure, while the working temperature has a relatively minor impact.

Accordingly, although the typical research object like nozzles and hydrofoils which can generate cavitation, has been thoroughly studied, the cavitation model has undergone a series of modifications and optimizations.

Similarly, the cavitation phenomenon within fluid machinery such as pumps, turbines, needle valves, and cut-off valves has been investigated. However, there has been limited investigation into cavitation phenomena occurring in butterfly valves.

Researchers conducted numerical simulations utilizing Large Eddy Simulation combined with a Schnerr-Sauer cavitation model (Schnerr et al., 2001) which is modified to reveal the dynamic evolution mechanism of cavitation. These simulations explored how cavitation evolves within a butterfly valve model under varying regulatory conditions. The analysis covered the cavitation cycle, including its generation, development, and collapse. The vapor volume fraction, an indicator of cavitation volume, was obtained and thoroughly discussed for each valve opening position. The impact of cavitation evolution on the flow field was investigated by analyzing the disturbance coefficient at various valve opening degrees. A comparative analysis of the distribution and structural characteristics unveiled the connection between cavitation and vortices.

2. NUMERICAL METHODS

2.1 Governing Equations

The multiphase flow model employs the mixture model, and the volume fraction formulation is implicit. This study excludes considerations of interphase heat transfer and compressibility; therefore, the governing equations primarily comprise the continuity equation and the momentum conservation equation.

The Continuity equation is as follows:

$$\frac{\partial \rho}{\partial t}+\rho\frac{\partial u_i}{\partial x_i}=0 \tag{1}$$

where t is time; ρ is the fluid density; u is velocity; i represents different dimensions of the fluid movement, which in three-dimensional space i=1, 2, and 3.

The following is the momentum conservation equation:

$$\rho\frac{\partial u_j}{\partial t}+\rho u_i\frac{\partial u_j}{\partial x_i}=-\frac{\partial p}{\partial x_j}-\frac{\partial \tau_{ij}}{\partial x_i}+\rho g_j \tag{2}$$

where p is the fluid pressure; g is the acceleration of gravity; τ_{ij} is the viscous stress tensor. Its formula is as follows:

$$\tau_{ij}=-\mu\left(\frac{\partial u_j}{\partial x_i}+\frac{\partial u_i}{\partial x_j}\right)+\frac{2}{3}\delta_{ij}\mu\frac{\partial u_k}{\partial x_k} \tag{3}$$

where μ is dynamic viscosity.

2.2 Turbulence Model

One of the most precise methods for simulating turbulence is LES. LES theory states turbulence consists of vortices of varying scales. Large-scale pulsations, possessing significant energy and momentum, predominate in the kinetic energy and energy transport of turbulent pulsations, while the dissipation of turbulent kinetic energy primarily occurs in small-scale pulsations (Kolmogorov, 1991). LES focuses on computing the turbulence fluctuations at larger scales while filtering out the smaller-scale fluctuations. LES utilizes a modeling approach known as the Subgrid-Scale Model which accommodate the effects of these smaller-scale fluctuations on the larger ones. After filtering the smaller-scale fluctuations, the following is the equation of large-volume vortex:

$$\frac{\partial}{\partial t}(\rho\overline{u_i})+\frac{\partial}{\partial x_j}(\rho\overline{u_i}\,\overline{u_j})=-\frac{\partial \bar{p}}{\partial x_i}+\mu\frac{\partial}{\partial x_j}\left(\frac{\partial \overline{u_i}}{\partial x_j}+\frac{\partial \overline{u_j}}{\partial x_i}\right)-\frac{\partial \tau_{ij}}{\partial x_j} \tag{4}$$

$$\tau_{ij}-\frac{1}{3}\tau_{kk}\delta_{ij}=-2\mu_t\bar{S}_{ij} \tag{5}$$

where $\bar{p}$ is the far-field pressure; τ_{ij} is Subgrid stress; $\bar{S}_{ij}$ is strain rate tensor at decomposition scale; μ_t is turbulent vortex viscosity; $\bar{u}$ is the far-field velocity.

Nicoud et al. (2001) proposed the WALE SubGrid-Scale Model for the subgrid stress equation to yield a closed-form solution. The relevant parameters are obtained as follows:

$$\mu_t=\rho L_s^2\frac{\left(S_{ij}^d S_{ij}^d\right)^{3/2}}{\left(\overline{S_{ij}}S_{ij}^d\right)^{5/2}+\left(S_{ij}^d S_{ij}^d\right)^{5/4}} \tag{6}$$

where L_s and S_{ij}^d are determined as follows:

$$L_s=min\left(\kappa d, C_w V^{1/3}\right) \tag{7}$$

$$S_{ij}^d=\frac{1}{2}\left(\bar{g}_{ij}^2+\bar{g}_{ji}^2\right)-\frac{1}{3}\delta_{ij}\bar{g}_{kk}^2,\ \bar{g}_{ij}=\frac{\partial \overline{u_i}}{\partial x_j} \tag{8}$$

C_w = 0.325.

2.3 Cavitation Model

The Schnerr-Sauer cavitation model was selected, and the formula of the source term is as follows:

$$\dot{m}^+=\frac{\rho_v\rho}{\rho}\alpha_v(1-\alpha_v)\frac{3}{R_0}\sqrt{\frac{2}{3}\frac{max(p_v-p,0)}{\rho_l}} \tag{9}$$

$$\dot{m}^-=\frac{\rho_v\rho}{\rho}\alpha_v(1-\alpha_v)\frac{3}{R_0}\sqrt{\frac{2}{3}\frac{max(p-p_v,0)}{\rho_l}} \tag{10}$$

This study assumes that the quantitative density of bubbles is n_0 = 11, aligns with the experimental data (Morgut et al., 2011).

2.4 Cavitation Radius Equation

For the cavitation radius calculation, this study proposes introducing Sauter Mean Diameter (SMD) to characterize the cavitation radius.

The specific expression is as follows:

$$R_B=\frac{0.034\left(\frac{\rho_L}{\rho_v}\right)^{1.326}}{Re^{0.324}\left(Ja_{sub}+\frac{149.2\left(\frac{\rho_L}{\rho_v}\right)^{1.326}}{Bo^{0.478}\,Re^{1.6}}\right)}\sqrt{\frac{\sigma}{(\rho_l-\rho_v)}} \tag{11}$$

where R_B is the bubble radius; B_o is the boiling number of the liquid phase; Ja_{sub} is the dimensionless constant of liquid subcooling; σ is the surface tension.

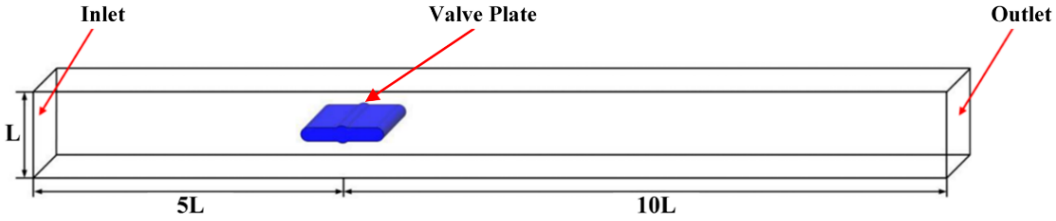

Fig. 1 Computational domain

3. BOUNDARY CONDITIONS AND VALIDATION

3.1 Computational Model And Boundary Conditions

Water serves as the liquid medium in this study, having a temperature of 300K, a density of 998.2 kg/m³, and a saturated vapor pressure of 3540 Pa, a viscosity of 0.001003 kg/(m·s). The model features a square pipe with a diameter of 10 × 10 mm. To ensure that fluid flow development at the inlet and outlet pipelines remains unaffected by boundary conditions and facilitates full cavitation development, a flow zone of 5L precedes the butterfly valve, and a 10L flow zone follows it, as illustrated in Fig.1. A structural mesh discretizes the fluid domain, as depicted in Fig. 2, to improve the accuracy of the numerical calculations.

Generally, the butterfly valve maintains a constant degree of opening to ensure continuous fluid transport in the pipeline at a fixed flow rate. The opening degree of the valve determines the speed. Based on the flow characteristic curve, the butterfly valve inlet conditions are obtained. The inherent flow characteristics of the butterfly valve (Yang, 1992) describe the relationship between the relative flow (q=Q/Q_{max}) and the valve core relative travel distance (l=a/a_{max}) when the pressure drop across the valve remains constant, which can be expressed by the following function:

$$q = \frac{Q}{Q_{\max}} = R^{\left(\frac{a}{a_{max}}-1\right)} = R^{(l-1)} \tag{12}$$

$$a_{max} = 90° \tag{13}$$

where Q is the flow rate (m³/h) at an opening degree is a (°); Q_{max} is the flow rate at the maximum opening degree; a_{max} is the valve maximum opening degree.

In addition, R signifies the valve inherent adjustable ratio, defined as the ratio of maximum to minimum flow rates under a constant pressure drop. For this butterfly valve, the inherent adjustability ratio is R = 30.

After determining the inlet velocity at different openings, taking an opening of 100% as an example, the valve inlet is set as the velocity-inlet in ANSYS-Fluent, the value is 18.5 m/s. The outlet condition is designated as the pressure outlet, and its value is an atmospheric pressure. The butterfly valve surface and the pipe wall surface adopt non-slip wall conditions. PISO is selected for the pressure-velocity coupling method, which is better suited for transient numerical simulation. For the discrete format, the gradient was calculated using the Least squares-based method, the pressure was obtained by

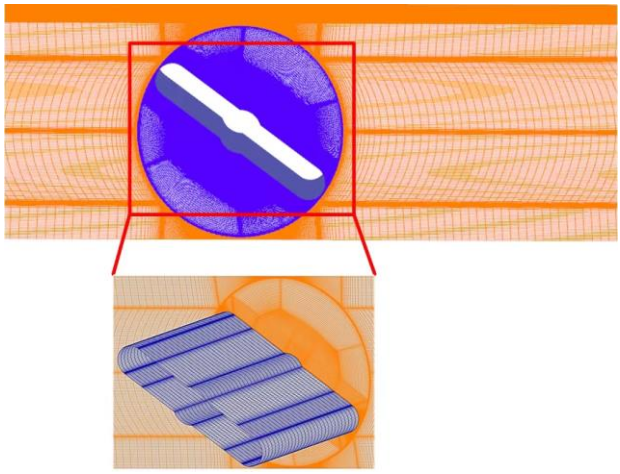

Fig. 2 Computational grids

PRESTO, Bounded Central Differencing was used for the momentum scheme, and Bounded Second Order Implicit was chosen for the transient formulation. To ensure calculation accuracy, a time step of 2×10^{-5} seconds was determined according to the Courant number criterion.

3.2 Experimental Device and Procedure

The actual diagram of the experimental device (Zhang et al., 2024) is shown in Fig. 3, and the structural diagram is presented in Fig. 4. The experimental device primarily consists of two water storage tanks, pipelines, safety valves, cut-off valves, butterfly valves, high-speed cameras, air compressors, and pressure-temperature sensors.

Fig. 3 Actual diagram of the experimental device

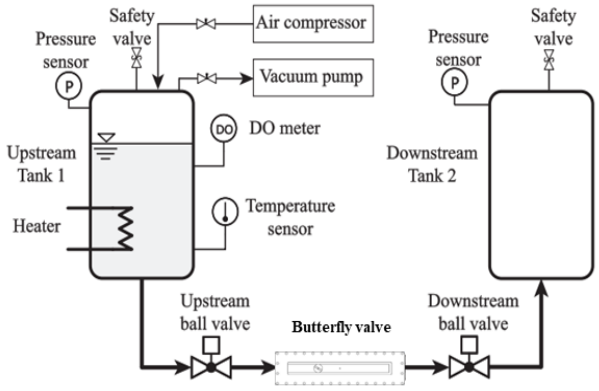

Fig. 4 Structural diagram of the experimental device

Before the experiment begins, water completely fills the storage tank on the left. The ball valve controlling the inlet and outlet of the pipeline between the two water storage tanks is opened, along with the upstream and downstream ball valves, for 1–2 seconds, allowing the water in the left tank to flow naturally through the pipeline into the right tank. This procedure helps evacuate the air in the channel and submerge the butterfly valve in water. The pipeline where the butterfly valve is located measures 10 mm × 10 mm. The butterfly valve opening is adjustable, and the section is visualized through a piece of organic glass installed to enhance the observation and recording of experimental phenomena. Pressure sensors with high precision, boasting an accuracy of 0.1%, are installed at both ends of the visualization setup: the inlet and outlet sections. Upon completion of the exhaust process, the ball valve adjacent to the butterfly valve's left side is sealed shut, air compressor linked to the left tank is start-up, and the inlet pressure sensor's value is monitored. When the experimental conditions are met, the left ball valve is opened. Simultaneously, the high-speed camera placed in front of the visualization section is activated to record the cavitation phenomenon at a shooting frame rate of 2200 fps. The high-speed camera and pressure sensor are connected to the computer to record and store the changes in cavitation and inlet and outlet pressures during the experiment.

3.3 Validation

The mesh number significantly impacts the accuracy of numerical simulations, therefore, ensuring grid independence is indispensability to guarantee that calculation accuracy remains unaffected by changes in the mesh number.

This study compared five sets of grids between 2 million and more than 5 million, by examining the flow coefficient and the drag coefficient.

$$Kv = 10Q\sqrt{\frac{\rho}{\Delta P}} \tag{14}$$

$$C_d = \frac{2\Delta P}{\rho v^2} \tag{15}$$

where ΔP is the pressure drop (Pa); ρ is the density of the liquid (kg/m^3); Q is the flow rate (m^3/h); v is the flow velocity (m/s).

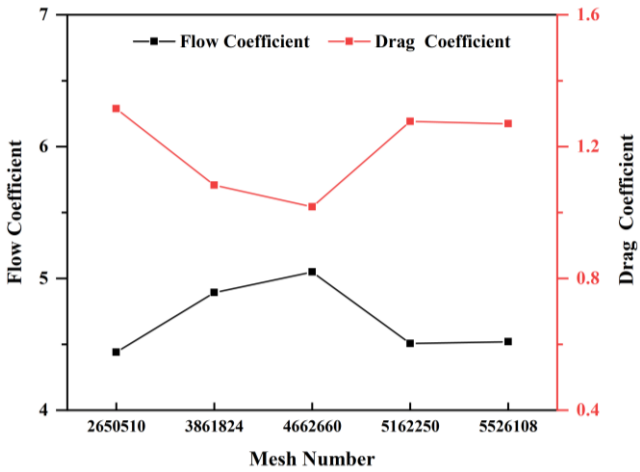

Fig. 5 Flow and drag coefficients at different mesh numbers

Figure 5 illustrates a clear trend: as the mesh numbers rises, both the flow and drag coefficients approach a stable state. Both coefficients converge to a stable value when the grid count reaches 5.16 million. This study selects the 5.16 million grid configuration for numerical simulations to optimize computational resources and prevent unwarranted resource consumption, ensuring accuracy and efficiency.

An experimental study of cavitation in butterfly valves was conducted. Figure 6 displays a comparison of the cavitation distribution between the experimental results and the numerical simulation for a typical period. Due to cavitation has the periodicity apparently, the evolution of cavitation from generation to collapse is defined as a period T. T is divided equally to examine the state of cavitation at various stages within the period. At t=1/6T, two clusters of cavitation are generated above the butterfly valve. By 2/6T, the cavitation clusters enlarge and develop continuously until 3/6T, when the cavitation close to the top of the valve core has progressed to the middle part of the valve, and the cavitation at the end has collapsed. At 4/6T, the cavitation group has crossed the butterfly valve shaft diameter and enlarged, initiating a new cavitation cycle at the top of the core. The cavitation distribution pattern at 4/6T resembles that at 1/6T. At 5/6T, the cavitation extends further toward the end of the development, showing a tendency to collapse. The cavitation has contracted to the end of the valve then collapsed into small bubbles by 6/6T. The accuracy of the numerical simulation method can be affirmed by observing the small disparity between the numerical simulation outcomes and the experimental results.

4. RESULTS AND DISCUSSION

4.1 Cavitation Distribution

Researchers acquired data on vapor volume fraction distribution at varying degrees of valve opening to comprehensively grasp the detailed developmental stages of cavitation. Figure 7 indicates that the vapor volume fraction distribution was obtained during a typical period when valve opening degree is 60%. When t = 0.0998 s, a minuscule cavitation starts to form at the upper surface,

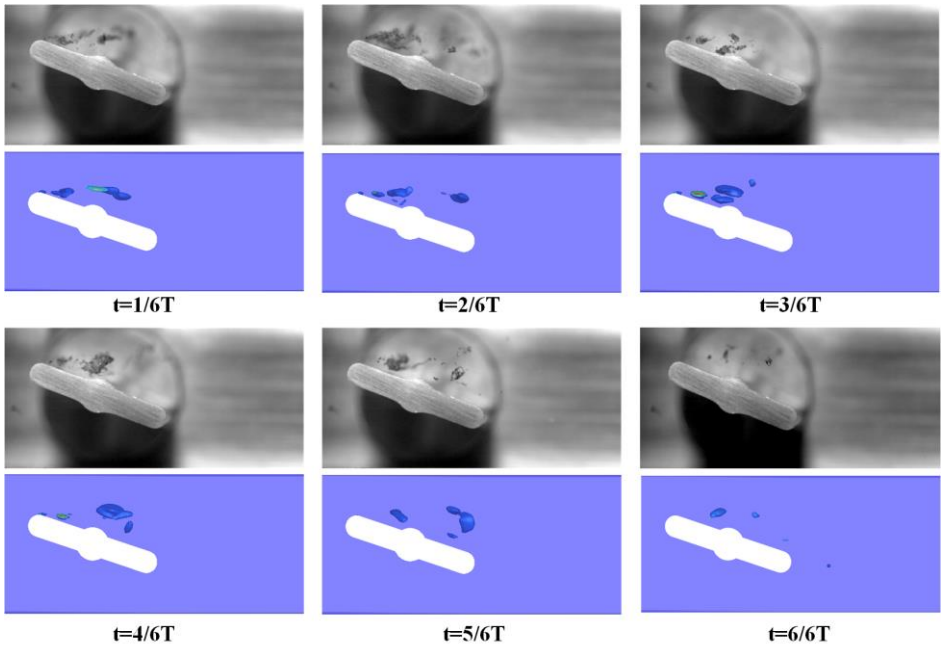

Fig. 6 Comparison of experimental and numerical results of cavitation distribution

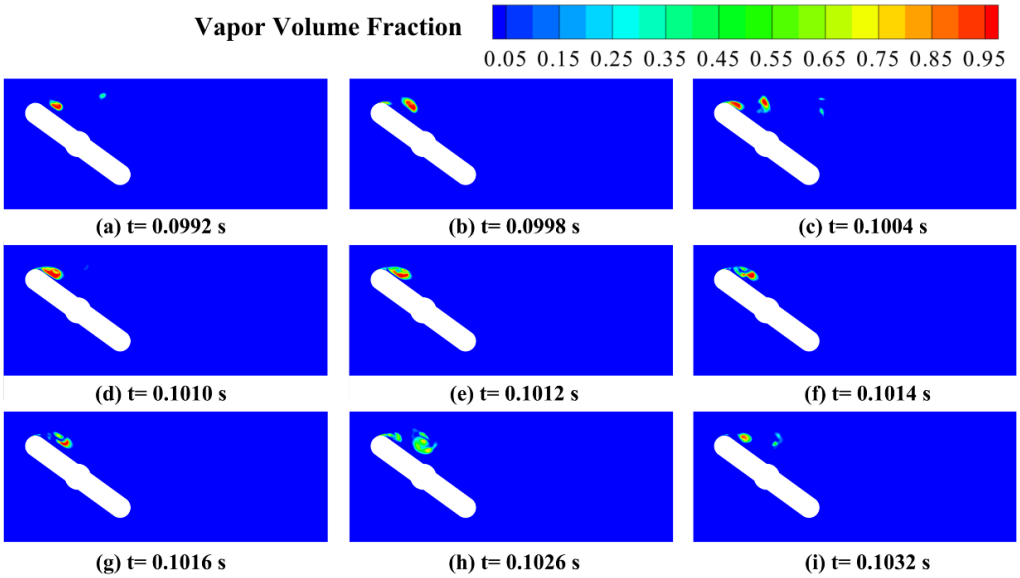

Fig. 7 Cavitation distribution at 60% opening degree

with its volume steadily enlarging over time. By t = 0.1004 s, cavitation from the preceding cycle shrinks, while cavitation in the present cycle grows. At t = 0.1012 s, the bubble starts to fracture and separate from the interior, dividing into several tiny bubbles and splitting at t = 0.1014 s. The tiny bubbles adjacent to butterfly plate collapse altogether, the bubbles volume at the rear gradually decreases. When t = 0.1026 s, the cross-sectional area of the flow passage widens, leading to an increase in pressure and a gradual reduction in the vapor phase content within the cavitation, which diffuses and collapses gradually. In addition, new cavitation continuously generates on the butterfly plate surface, extending rearward over time.

The cavitation distribution when the opening degree is 80%, depicted in Fig 8. At t = 0.3334 s, shedding cavitation is generated both above and below the valve plate. The cavitation bubble generated at the upper part of the valve core gradually separates from the butterfly plate and fuses into a large bubble. At t = 0.3348 s, the bubbles originating from the terminus of the butterfly plate fuse, then gradually compress and finally collapse completely. Periodic shedding reveals that the cavitation formed at the front of the valve plate is larger, with only a small amount of cavitation formed at the terminus, fusing with the cavitation at the upper end in the later stage.

At a valve opening degree of 100%, the cavitation distribution, as illustrated in Fig. 9, begins. Due to the horizontal orientation of the plate, cavitation bubbles form on both its upper and lower surfaces, and the cavitation

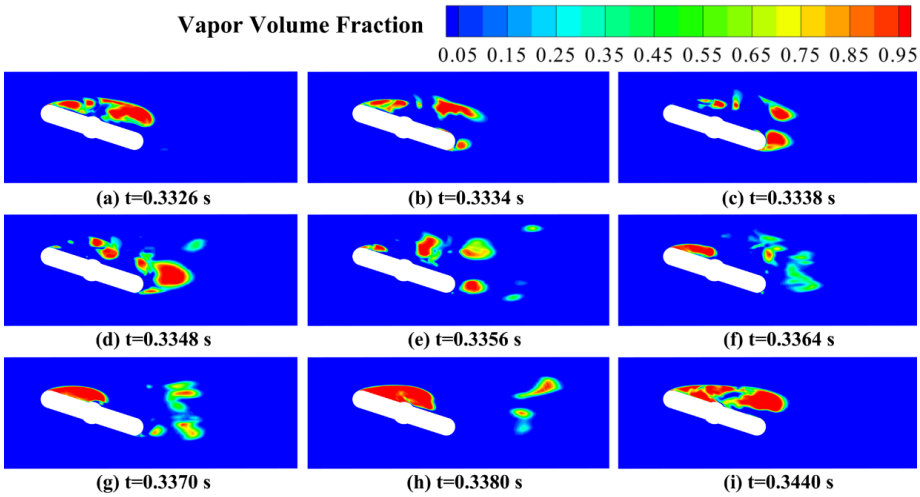

Fig. 8 Cavitation distribution at 80% opening degree

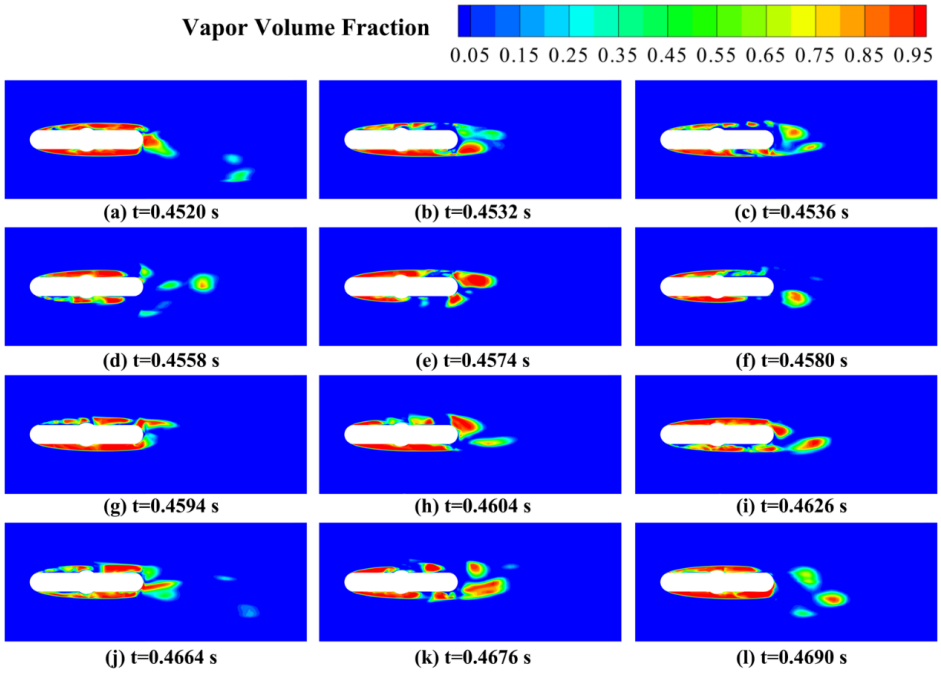

Fig. 9 Cavitation distribution at 100% opening degree

bubbles exhibit a uniform size. Despite the symmetrical structure of the butterfly plate, the cavitation flow field displays asymmetry. This phenomenon occurs due to flow separation behind the butterfly plate, and the vortex asymmetry leads to alternating cavitation shedding.

The study measures the pressure distribution at various valve opening degrees to comprehend the pressure dynamics within the cavitation flow field. Figure 10 shows the pressure distribution corresponding to the opening degree of 60%. When t = 0.1004 s, a reduced pressure area is noted on the rear section of the upper surface. Simultaneously, some low-pressure areas also appear within the flow domain adjacent to the rear, and the closer to the surface of the valve plate, the more concentrated the low-pressure area is. At t = 0.1012 s, the low-pressure area recedes and disappears in the flow field. The low-pressure area on the surface of the plate is expanding bit by bit. When t = 0.1026 s, the low-pressure area on the plate surface gradually moves along the flow direction and separates from the butterfly plate surface. In addition, new low-pressure area appears on the butterfly plate surface. Finally, at t = 0.1032 s, like the previous low-pressure area, the new low-pressure area also begins to break away from the surface and move backward gradually. The pressure distribution at four specific instances illustrates that the pressure preceding the plate surpasses that found in its rear. The pressure behind the valve is generally about 8.0×10^4 Pa. The pressure value diminishes only in the low-pressure area, typically falling below 2.0×10^4 Pa.

The pressure distribution depicted in Fig. 11 corresponds to the opening degree of 80%. Contrasting with the pressure distribution when the opening degree is 60%, as the opening degree increases, a decrease in pressure difference within the valve is observed. A high-

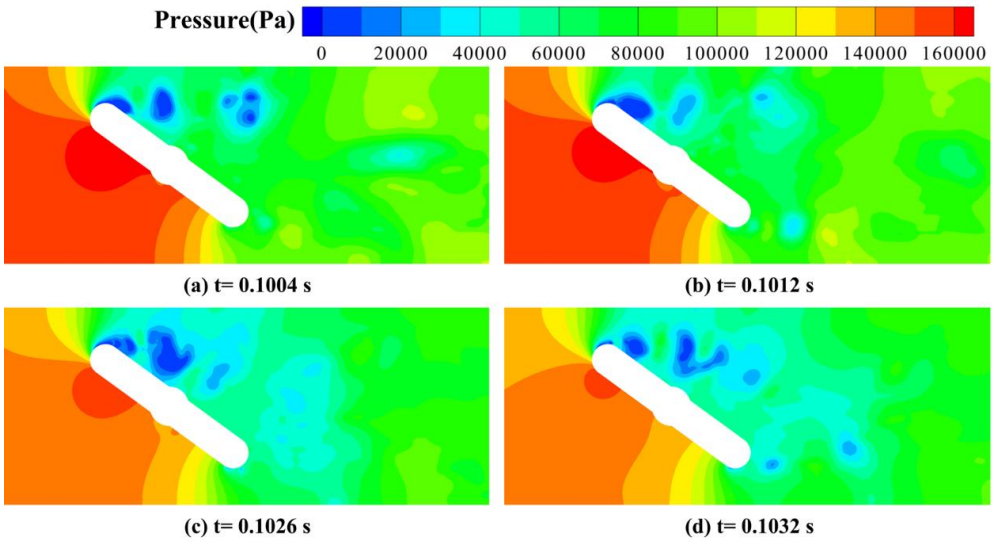

Fig. 10 Pressure distribution at 60% opening degree

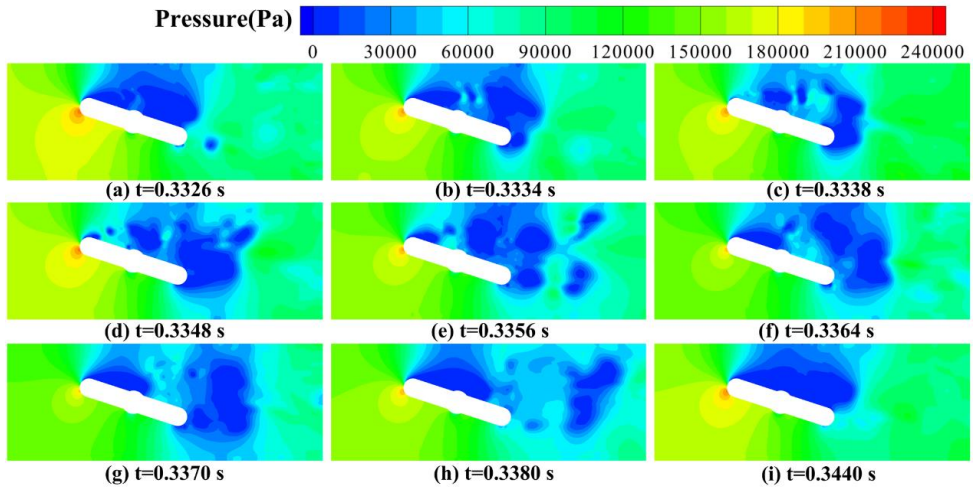

Fig. 11 Pressure distribution at 80% opening degree

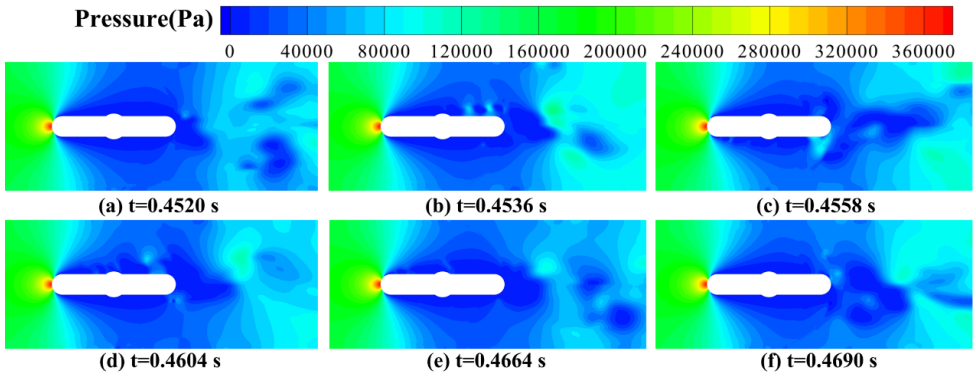

Fig. 12 Pressure distribution at 100% opening degree

pressure area appears at the uppermost part of the valve core. Resembling the pressure distribution observed at 60% opening degree, an area of low pressure, characterized by an uneven distribution, becomes evident at the back of the butterfly plate. The rearward extension of the newly low-pressure region persists, and the low-pressure area generated at the upper part of the butterfly plate in the previous stage gradually dissipates. Due to a pressure gradient, the high-pressure area tends to move toward the low-pressure area. Finally, the pressure gradient decreases gradually, and a gradual tendency towards even distribution of the pressure.

Figure 12 depicts the pressure distribution corresponds to the opening degree of 100%. Similar to the pressure

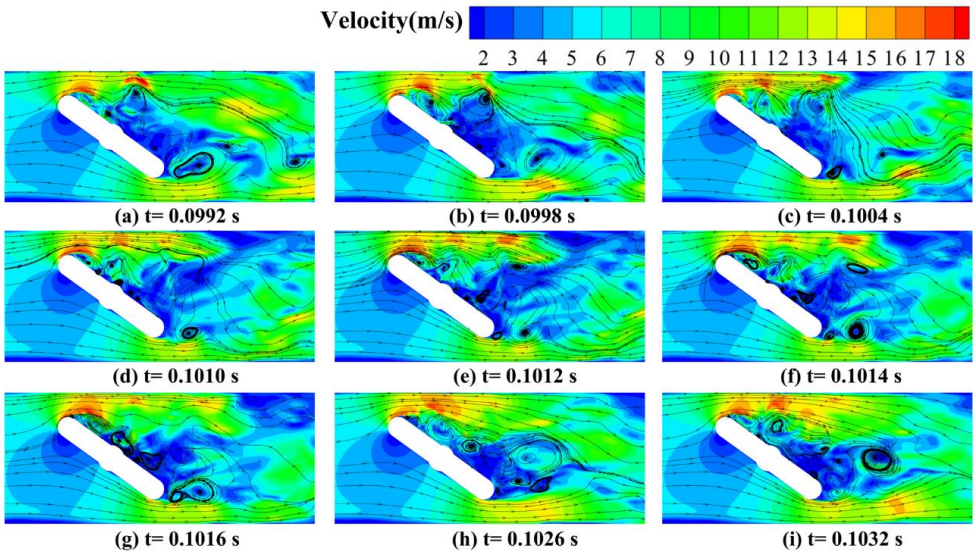

Fig. 13 Velocity contour and streamline at 60% opening degree

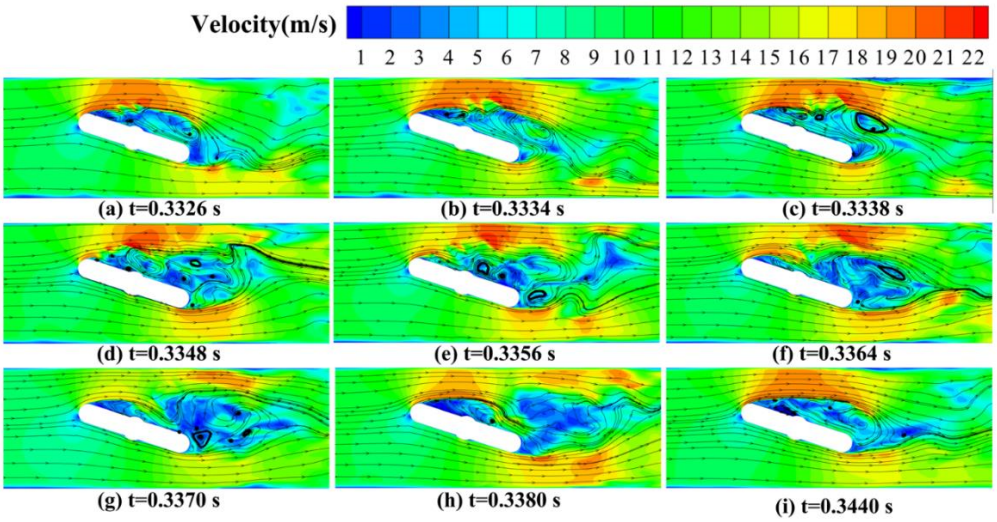

Fig. 14 Velocity contour and streamline at 80% opening degree

distribution observed at 80%, a high-pressure area emerges at the uppermost part of the valve core. This phenomenon stems from the presence of the plate; the fluid velocity is suppressed, and a significant accumulation of fluid happens at the front end of the plate, leading to a substantial increase in pressure. At t = 0.4536 s, the low-pressure area above the plate separates. At t = 0.4558 s, the low-pressure area beneath the plate separates, illustrating the alternating disappearance of the low-pressure area.

The study explores the velocity contour and streamlines at various opening degrees to research the mechanism of periodic cavitation shedding. The velocity contour and streamline when the opening degree is 60% are depicted in Fig. 13. At t = 0.0992 s, two vortices with opposite rotations are above and below the butterfly plate. The vortices extend backward with the movement of cavitation, and the increase in cavitation accompanies the increase in vortex radius when t = 0.0998 s. Simultaneously, numerous small vortices appear on the lower and rear sides of the butterfly plate, where no cavitation occurs. At t = 0.1012 s, the vortex radius associated with cavitation continues to enlarge, and the velocity flow field becomes more unstable. Although a vortex also appears below the butterfly plate, no cavitation occurs there, indicating that factors other than the vortex affect cavitation. The flow torque near the vortex cavity is clockwise, reflecting the fluid's tendency to occupy the entire flow field as the cross-sectional area increases. Consequently, the fluid above the flow channel tends to flow toward the center of the valve plate, resulting in re-entrant flow and the separation of the cavitation from the valve plate surface. The changes in cavitation shedding and velocity flow field suggest a strong correlation between cavitation shedding, re-entrant flow, and vortex formation.

The velocity contour and streamline when the opening degree is 80% are depicted in Fig. 14. At t = 0.3326 s, two vortices with a moderate vortex disorder exist above the butterfly plate. Cavitation diminishes due to increased

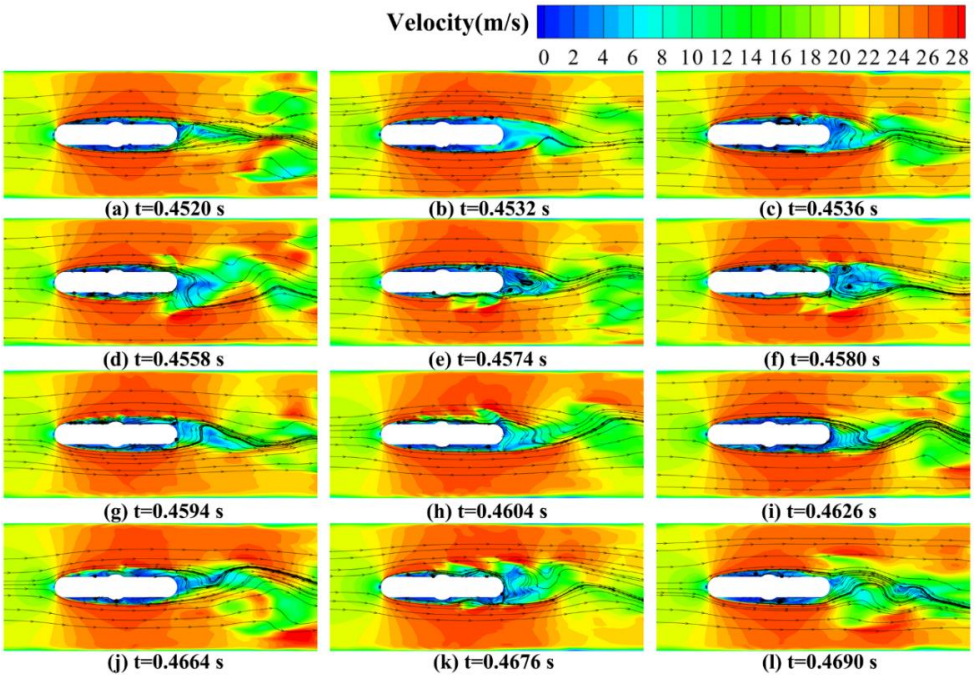

Fig. 15 Velocity contour and streamline at 100% valve opening degree

vortex instability at t = 0.3334 s and t = 0.3338 s. Subsequently, a new cavitation bubble forms above the butterfly plate, and a corresponding new vortex appears above the butterfly plate in the velocity flow field.

The minor vortex in the flow field has essentially disappeared at t = 0.3364 s, indicating the complete collapse of sporadic cavitation in the flow field. In the meantime, the cavitation forming above the valve plate increases, yet it does not detach; the corresponding vortex instability shows little change, and the flow field disorder diminishes. At t = 0.3440 s, the flow field becomes highly disorganized again due to the cloud cavitation shedding, resulting in the emergence of an instability vortex near the butterfly plate.

The velocity contour and streamline when the opening degree is 100% are depicted in Fig. 15. As the butterfly plate becomes horizontal, the flow field starts to symmetrize, the upper and lower regions of the butterfly plate become the high-speed and low-pressure regions. In the wake area at the tail of the butterfly plate, due to the hindrance of the valve plate, resulting in a reduced flow velocity within this region. Large and small vortices can be observed throughout the entire cycle. This phenomenon is the primary cause of cavitation, fission, and shedding. In addition, by analyzing the vortex count on both sides of the butterfly plates, it is evident that there is a noticeable disparity in the number of vortices between the two sides. Although the geometric model is symmetric, the vortices are asymmetric, and the vortex number on the two sides surfaces alternates. This asymmetry explains why the cavitation shedding of the upper and lower butterfly plates does not occur simultaneously.

4.2 Evolution Process of Cavitation

For the sake of explore deeper the understanding of cavitation formation and evolution mechanisms within a butterfly valve at fixed opening degrees, this study also investigates the cavitation evolution process under varying degrees of valve openings to enhance comprehension of how cavitation is influenced by the opening degree and the inlet velocity.

4.2.1 Analysis of Cavitation Time Sequence Development

Figure 16 displays the change of vapor volume fraction, which is defined as:

$$V_b = \sum_{i=1}^{n} \alpha_i V_i \tag{16}$$

In the above formula, n is the number of all grids, α_i is the vapor volume fraction of each computation element, V_i is all volumes of each computation element.

When the opening degree sets to 30%, 40%, and 50%, the periodicity of cavitation becomes more pronounced. However, at opening degrees of 60%, 70%, 80%, 90%, and 100%, this periodic phenomenon weakens. Observations of the cavitation volume variation over time at larger opening degrees reveal significant peaks, likely because the cavitation bubbles generated at the upstream and downstream ends oscillate at the same frequency, growing and detaching simultaneously.

4.2.2 Analysis of cavitation Characteristics

To better and more thoroughly analyze the periodic changes in the butterfly valve at fixed opening degrees, this paper introduces a combined coefficient that reflects the impact of the rotation angle and operating conditions on cavitation. The formula for this coefficient is described as follows:

$$\phi = \frac{\sigma_c}{2(1-\alpha)+\varepsilon} \tag{17}$$

$$\sigma_c = \frac{P_\infty - P_v}{\frac{1}{2}\rho U_\infty^2} \tag{18}$$

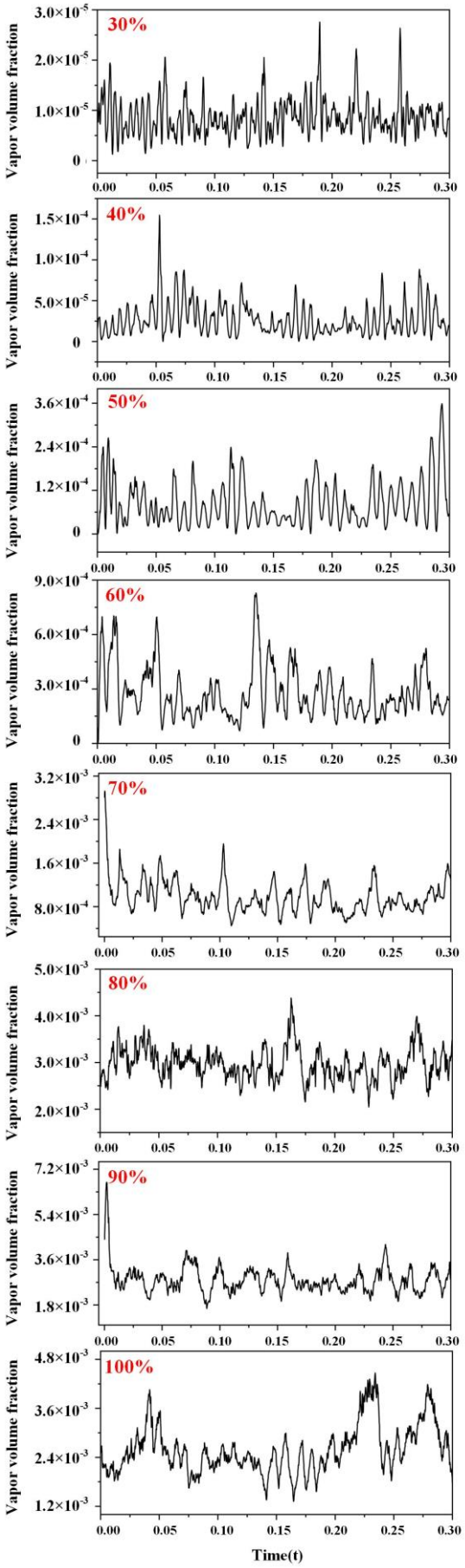

Fig. 16 The change of vapor volume fraction with time

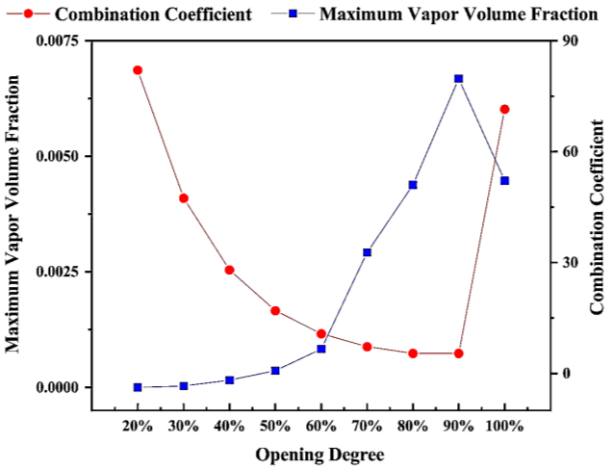

Fig. 17 Maximum cavitation volume and combination coefficient

where σ_c is cavitation number which is a dimensionless number proposed to describe the degree of cavitation occurrence; α is opening degree (α=a/a_{max}); ε is correction factor, where in this study ε = 0.008. P_∞ represents far-field pressure, P_v represents saturated vapor pressure, ρ represents liquid density, U_∞ represents the far field velocity.

Figure 17 demonstrates the investigation into the relationship between the valve opening degree and variations in both the maximum vapor volume fraction and the combination coefficient. The findings suggest an initial increase followed by a decrease in the maximum vapor volume fraction as the opening degree increases. The peak occurs at an opening degree of 90%, where the rate of change also escalates. This pattern mirrors the trend seen in the equal percentage flow characteristic curve of the butterfly valve, illustrating the cavitation phenomenon's severity is strongly correlated with the opening and inlet velocity. A smaller combination coefficient corresponds to a greater cavitation volume fraction.

Upon reaching an opening degree of 60%, the rate of increase in the cavitation volume experiences a marked acceleration. This indicates that cavitation emerges on both sides of the plate after the valve reaches a 60% opening, thus elevating the volume fraction. The maximum vapor volume fraction at 90% opening degree can be put down to that while far field pressure doesn't increase significantly, the far field velocity rises sufficiently, enhancing cavitation intensity. Although the far-field pressure also rises at 100% opening degree, the increase in far-field velocity is less marked, which conversely leads to a decrease in cavitation intensity at this opening degree.

The cavitation shedding frequency obtained by FFT Fourier transform of cavitation volume fraction is shown in Fig. 18. At 20% opening degree, cavitation is virtually nonexistent owing to the low inlet velocity, with the frequency peaking at 30% opening. Subsequently, the shedding frequency decreases progressively. The cavitation shedding frequency reaches its minimum when the valve opening is 60%. As the opening widen, a modest peak emerges. The bilateral falling-off phenomenon is not

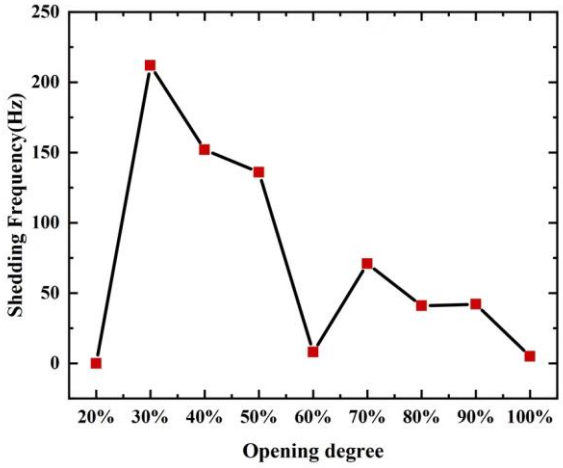

Fig. 18 Shedding frequency of cavitation

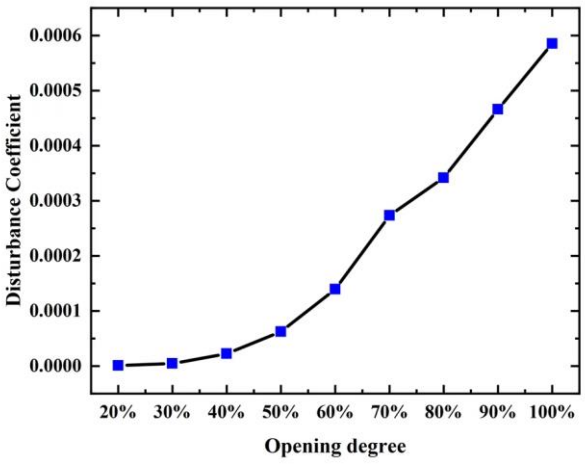

Fig. 19 Disturbance coefficient

pronounced at 60% opening degree, and the cavity at the butterfly valve's end sheds irregularly, not occurring in every cycle. Thus, when analyzing the shedding frequency through Fourier transform, no significant peak amplitude is observed. It is hypothesized that the period is extended in the periodic variation, resulting in a reduced shedding frequency. Upon widening the opening degree, the fluid velocity at the inlet alters, leading to a highly regular pattern of cavitation shedding at the end of the plate. Hence, variations in the shedding frequency of cavitation become markedly evident. The decline in shedding frequency is attributed to the increased intensity of cavitation changes, which involve cavitation with a larger cavitation volume fraction. During the evolution of cavitation, the expansion and collapse of cavities necessitate a prolonged duration, extending the time cycle for cavitation changes and subsequently decreasing the shedding frequency.

Finally, the influence of cavitation development at various opening degrees is examined. In this study, a coefficient is defined to quantify the extent of flow field disruption caused by variations in cavitation which is called the disturbance coefficient (ξ):

$$\xi = \sqrt{\frac{\sum_{i=1}^{n}(V_b^i - \overline{V_b})^2}{n}} \tag{19}$$

where n is the number of samples; V_b^i is the vapor volume fraction; $\overline{V_b}$ is the average vapor volume fraction.

The disturbance coefficient as shown in Fig. 19. It shows that the disturbance coefficient is roughly proportional to the valve opening.

4.3 Correlation Between Cavitation and Vortex

The Q criterion, a commonly utilized method for identifying vortices, was introduced by Hunt et al. (1988). It can be represented as follows:

$$Q = \frac{1}{2}(\|\boldsymbol{B}\|_F^2 - \|\boldsymbol{A}\|_F^2) \tag{20}$$

where A is the symmetric parts of the velocity gradient tensor. B is the antisymmetric parts of the velocity gradient tensor:

$$\boldsymbol{A} = \frac{1}{2}(\nabla \boldsymbol{v} + \nabla \boldsymbol{v}^T)$$

$$= \begin{bmatrix} \frac{\partial u}{\partial x} & \frac{1}{2}\left(\frac{\partial u}{\partial y} + \frac{\partial v}{\partial x}\right) & \frac{1}{2}\left(\frac{\partial u}{\partial z} + \frac{\partial w}{\partial x}\right) \\ \frac{1}{2}\left(\frac{\partial v}{\partial x} + \frac{\partial u}{\partial y}\right) & \frac{\partial v}{\partial y} & \frac{1}{2}\left(\frac{\partial v}{\partial z} + \frac{\partial w}{\partial y}\right) \\ \frac{1}{2}\left(\frac{\partial w}{\partial x} + \frac{\partial u}{\partial z}\right) & \frac{1}{2}\left(\frac{\partial w}{\partial y} + \frac{\partial v}{\partial z}\right) & \frac{\partial w}{\partial z} \end{bmatrix} \tag{21}$$

$$\boldsymbol{B} = \frac{1}{2}(\nabla \boldsymbol{v} - \nabla \boldsymbol{v}^T)$$

$$= \begin{bmatrix} 0 & \frac{1}{2}\left(\frac{\partial u}{\partial y} - \frac{\partial v}{\partial x}\right) & \frac{1}{2}\left(\frac{\partial u}{\partial z} - \frac{\partial w}{\partial x}\right) \\ \frac{1}{2}\left(\frac{\partial v}{\partial x} - \frac{\partial u}{\partial y}\right) & 0 & \frac{1}{2}\left(\frac{\partial v}{\partial z} - \frac{\partial w}{\partial y}\right) \\ \frac{1}{2}\left(\frac{\partial w}{\partial x} - \frac{\partial u}{\partial z}\right) & \frac{1}{2}\left(\frac{\partial w}{\partial y} - \frac{\partial v}{\partial z}\right) & 0 \end{bmatrix} \tag{22}$$

where $\|\cdot\|_F^2$ is norm.

Generally, it was considered a vortex when $Q > 0$. The second condition is that the vortex region pressure is lower than the ambient pressure. In actual situations, only the region of $Q > Q_{threshold}$ can be defined as a vortex.

The Q criterion, which captures the three-dimensional structure of vortices, is introduced to deepen the understanding of the cavitation mechanism's evolution in the butterfly valve. This section primarily investigates the distribution of cavitation in the horizontal direction at various valve openings and its temporal relationship with the structure of vortices.

Figure 20 depicts the evolution process of vortex and cavitation at 60% opening degree. The evolution of cavitation in the horizontal direction is not completely synchronous. This discrepancy is likely influenced by the wall adhesion effect. The cavitation bubbles that detach horizontally exhibit an inner concave shape, with the central area losing more cavitation than the areas on either side. This phenomenon can occur because the wall attachment effect causes the flow velocity in the central region to exceed that on the margins, facilitating easier detachment of central cavitation.

There is a correlation between the position of vortex and cavitation. The distribution of vortex structures, demonstrating spatial and temporal synchronization closely with the edge position of the cavitation. At t =

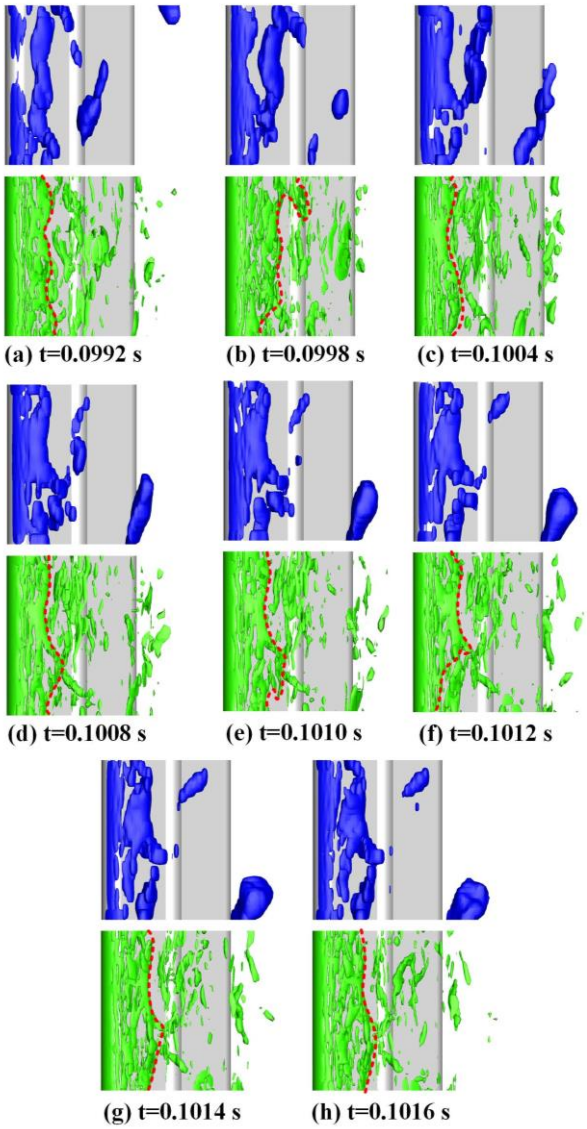

Fig. 20 Cavitation and vortex distributions at 60% opening degree

0.0992 s, some cavitation has just detached, displaying continuity in location with newly formed and recently detached cavitation. Cavitation is still attached on the both sides of the valve core, whereas the cavitation has almost entirely detached on the center of the valve core. Subsequently, at t = 0.0998 s, cavitation has grown that formed in the previous moment; however, the cavitation is thicker on the sides and thinner in the center, because the slower formation time of the central cavity. At t = 0.1004 s, the cavitation formed in the cycle begins to shed structures, initiating from the edge of one side horizontally. At t = 0.1008 s, on the horizontal edge opposite the valve core, cavitation begins to fracture. Simultaneously, cavitation from the previous cycle continues to develop backward. By t = 0.1010 s, it has collapsed into smaller bubbles within the flow field. The cavitation formed in this cycle has completely detached, forming crescent-shaped bubbles when t=0.1016s.

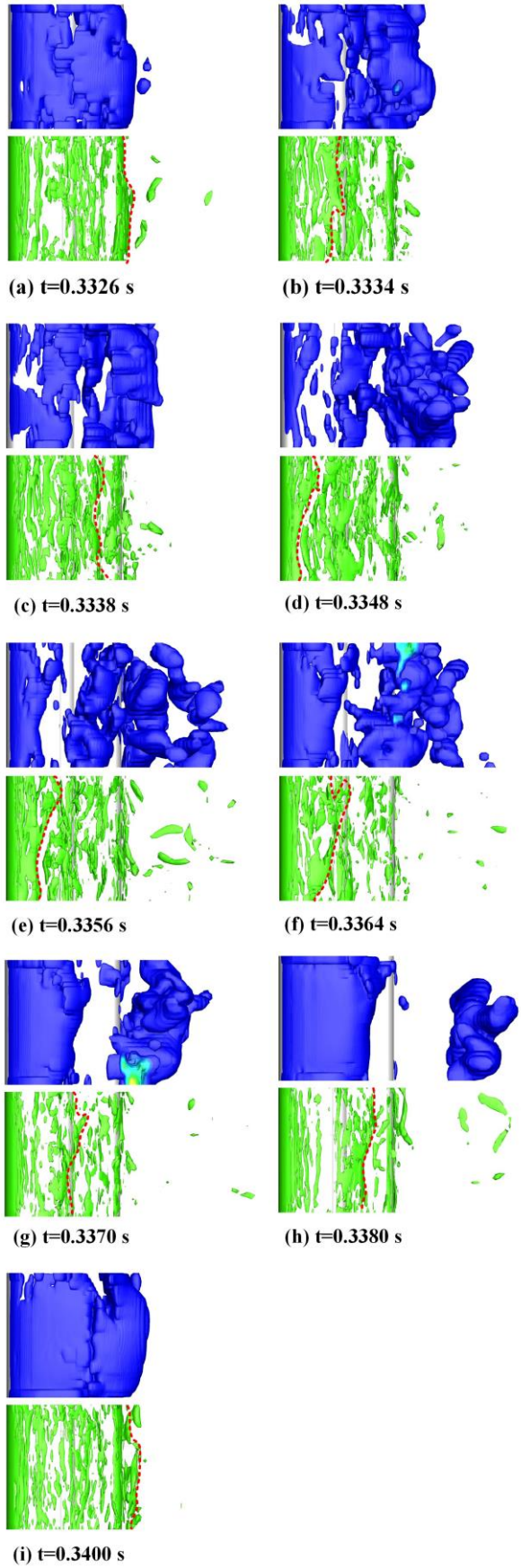

Fig. 21 Cavitation and vortex distributions at 80% opening degree

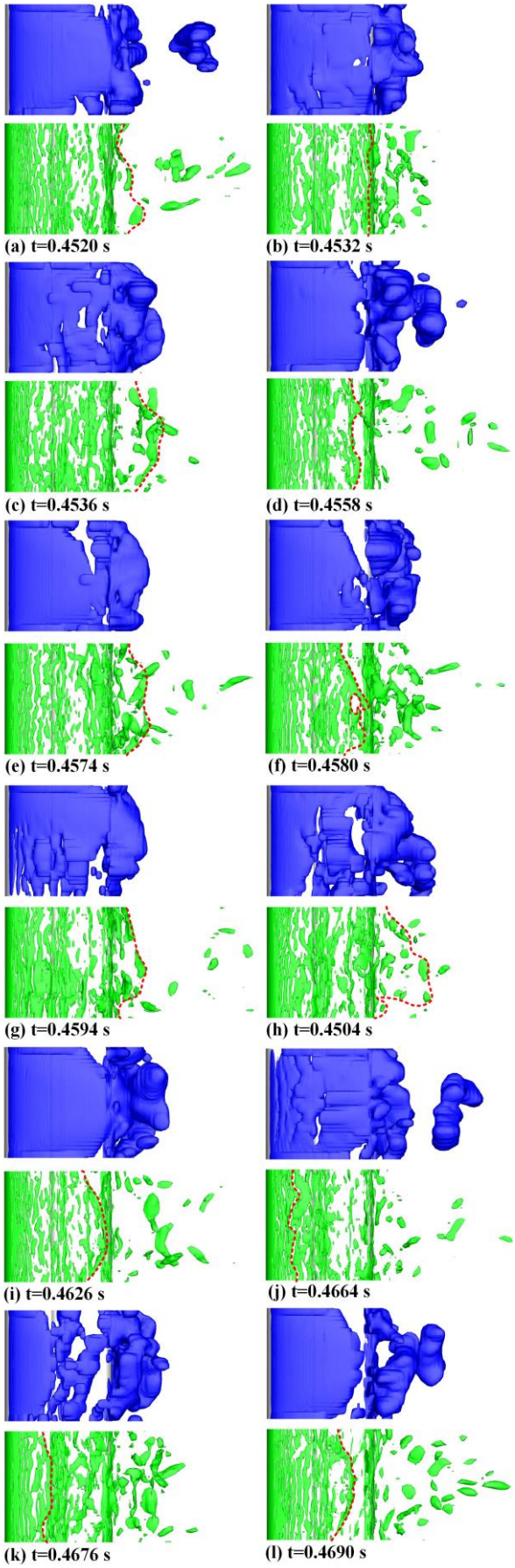

Fig. 22 Cavitation and vortex distributions at 100% opening degree

Figure 21 illustrates the distributions of cavitation and vortex at an opening degree of 80%. Compared to the 60% opening degree, the cavitation volume fraction at 80% is larger, with a more extensive distribution area and more drastic changes. The spatial distribution of the vortex structure correlates closely with the edge structure of cavitation, similar to the observations at 60% opening degree. This correlation confirms a strong connection between cavitation and vortex.

Finally, the study of cavitation and vortex distributions at an opening degree of 100%, as shown in Fig. 22, reveals that the horizontal distribution of cavitation remains relatively unchanged compared to other opening degrees. However, compared to Fig. 9, vertical changes in bubbles are significant. The larger vapor volume fraction under this condition consistently results in cavitation fractures, maintaining good continuity. When cavitation detaches from the butterfly plate, it does not disintegrate entirely but instead disconnects from back to front internally, close to the butterfly plate. In the cavitation periphery, complete disconnection is absent, and some adhesion persists. This persistence is likely because the fluid velocity in the distant field is high. If detachment occurs near the butterfly plate's surface, the pressure increases. Hence, during the phase exchange, there is a long and narrow area in the middle where the evaporation and condensation rates are equal, leading to the bridging of cavitation band adhesion. Upon detailed examination of the cavitation and vortex structures in the figure, like at other opening degrees, the trailing edge of the cavity generally aligns with the vortex structure, further verifying the synchronization of the spatial and temporal development of vortex and cavitation.

5. CONCLUSION

This study conducts a 3-D numerical simulation to research the dynamic cavitation evolution inside a butterfly valve model. The research considers various inlet velocities and valve opening degrees using LES coupled with an improved Schnerr-Sauer cavitation model. It is found that the cyclic progression of cavitation, encompassing three distinct phases, generation, development, and collapse. The period of cavitation evolution increases with the degree of opening. Similarly, the vapor volume fraction rises with the opening degree. The cavitation volume reaches the maximum, underscoring the substantial impact of both inlet velocity and valve opening on cavitation generation at an opening degree of 90%. Due to the influence of the dynamic evolution of cavitation, the turbulence within the flow field is heightened. In addition, the disturbance coefficient increases corresponding to the growth of cavitation volume. Cavitation is attached to the upper surface of the valve plate, where it tends to aggregate due to the resistance exerted by the valve shaft. The shedding frequency of cavitation decreases with the increases of opening degree. The shedding frequency of cavitation drop sharply at an opening degree of 60% because the shedding characteristics changed from unilateral to bilateral shedding. Consistent behavior is observed in both the spatial and temporal aspects of cavitation evolution and vortex movement by comparing cavitation and vortex in distribution and structure. The present studies obtained the distribution and characteristics of cavitation at

different valve opening degrees through a butterfly valve, revealing the dynamic evolution mechanism of cavitation, which is meaningful in providing a theoretical basis for designing processing valves to mitigate cavitation effects.

ACKNOWLEDGEMENTS

This research was funded by the National Natural Science Foundation of China (Grant No. 52222601), the Key Research and Development Program of Zhejiang Province (Grant NO. 2022C01140), and Zhejiang Sci-Tech University.

CONFLICT OF INTEREST

The authors have no conflicts to disclose.

AUTHORS CONTRIBUTION

Guang Zhang conceived and designed this research, and wrote the paper, **Xuan Wu** processed the results and wrote the paper, **Ze Yong Wu** and **Hao Tian Zhang** conducted simulation research, **Heuy Dong Kim** and **Xiao Yu He** revised the paper, **Zhe Lin** provided opinions on the paper. All authors read and approved the manuscript.

REFERENCES

Feng, X., Liu, Y., & Wang, B. (2023). Tip Leakage flow structures and its influence on cavitation inception for a NACA0009 hydrofoil. *Journal of Fluids Engineering, 145*(5), 0551203. https://doi.org/10.1115/1.4056941

Habibnejad, D., Akbarzadeh, P., Salavatipour, A., & Gheshmipour, V. (2022). Cavitation reduction in the globe valve using oblique perforated cages. A numerical investigation. *Flow Measurement and Instrumentation, 83*, 102110. https://doi.org/10.1016/j.flowmeasinst.2021.102110

Hunt, J. C. R., Wray, A. A., & Moin, P.(1988). Eddies, streams, and convergence zones in turbulent flows. *Center for Turbulence Research, Proceedings of the Summer Program, (1970)*, 193–208. Bibcode:1988stun.proc..193H

Kolmogorov, A. N. (1991). The local structure of turbulence in incompressible viscous fluid for very large reynolds numbers. *Proceedings: Mathematical and Physical Sciences, 434*(1890), 9-13. https://doi.org/10.1098/rspa.1991.0075

Kolovos, K. G., Koukouvinis, P., Mcdavid, R. M., & Gavaises, M. (2021). Transient cavitation and friction-induced heating effects of diesel fuel during the needle valve early opening stages for discharge pressures up to 450 MPa. *Energies, 14*(10), 2923. https://doi.org/10.3390/EN14102923

Kozák, J., Rudolf, P., Hudec, M., Štefan, D., & Forman, M. (2018). Numerical and experimental investigation of the cavitating flow within venturi tube. *Journal of Fluids Engineering, 141*(4), 041101. https://doi.org/10.1080/10236210490258034

Le, A. D., Okajima, J., & Iga, Y. (2019a). Modification of energy equation for homogeneous cavitation simulation with thermodynamic effect. *Journal of Fluids Engineering, 141*(8), 081102. https://doi.org/10.1115/1.4042257

Le, A. D., Okajima, J., & Iga, Y. (2019b). Numerical simulation study of cavitation in liquefied hydrogen. *Cryogenics, 101*, 29-35. https://doi.org/10.1016/j.cryogenics.2019.04.010

Li, J., Gao, Z., Wu, H., & Jin, Z. (2020). Numerical investigation of methodologies for cavitation suppression inside globe valves. *Applied Sciences, 10*(16), 5541. https://doi.org/10.3390/app10165541

Li, W., & Yu, Z. (2021). Cavitating flows of organic fluid with thermodynamic effect in a diaphragm pump for organic Rankine cycle systems L. *Energy, 237*, 121495. https://doi.org/10.1016/j.energy.2021.121495

Morgut, M., Nobile, E., & Biluš, I. (2011). Comparison of mass transfer models for the numerical prediction of sheet cavitation around a hydrofoil. *International Journal of Multiphase Flow, 37*, 620-626. https://doi.org/10.1016/j.ijmultiphaseflow.2011.03.005

Nicoud, F., Baggett, J. S., Moin, P., & Cabot, W. H. (2001). Large eddy simulation wall-modeling based on suboptimal control theory and linear stochastic estimation. *Physics of Fluids, 13*, 2968-2984. https://doi.org/10.1063/1.1389286

Schnerr, G. H., & Sauer. J. (2001). Physical and numerical modeling of unsteady cavitation dynamics. ICMF-2001: The 4th International Conference on Multiphase Flow, New Orleans, USA.

Sun, W., & Tan, L. (2020). Cavitation-Vortex-pressure fluctuation interaction in a centrifugal pump using bubble rotation modified cavitation model under partial load. *Journal of Fluids Engineering-transactions of the Asme, 142*(5), 051206. https://doi.org/10.1115/1.4045615

Tao, J., Lin, Z., Zhang, G., Su, J., & Zhu, Z. (2021). A numerical and experimental study of the time averaged and transient flow downstream of a butterfly valve. *Journal of Fluids Engineering, 144*(5), 051202. https://doi.org/10.1115/1.4052632

Wang, L., Ji, B., Cheng, H., Wang, J., & Long, X. (2020). One-dimensional/three-dimensional analysis of transient cavitating flow in a venturi tube with special emphasis on cavitation excited pressure fluctuation prediction. *Science China Technological Sciences, 63*, 223-233. https://doi.org/10.1007/s11431-019-9556-6

Wang, X., Zhang, J., Huang, Z., Wang, L., Li, W., & Lan, G. (2022). Large Eddy simulation on the cavitation flow and noise characteristics of a NACA0009 hydrofoil with different tip clearance sizes. *Journal of Fluids Engineering, 145*(1), 011204. https://doi.org/10.1115/1.4055542

Xue, R., Chen, L., Zhong, X.. Liu, X. F., Chen, S., & Hou, Y. (2019). Unsteady cavitation of liquid nitrogen flow in spray nozzles under fluctuating conditions. *Cryogenics, 97*, 144-148. https://doi.org/10.1016/j.cryogenics.2018.09.010

Yang, N., Okajima, J., & Iga, Y. (2023). Change in

cavitation regime on NACA0015 hydrofoil by heating the hydrofoil surface. *Journal of Fluids Engineering, 145*(7), 071201. https://doi.org/10.1115/1.4057004

Yang, Y. Q. (1992). *Valve Design Manual*. Beijing Machinery Industry Press. ISBN:7111035097.

Ye, W., Yi, Y., & Luo, X. (2020). Numerical modeling of unsteady cavitating flow over a hydrofoil with consideration of surface curvature. *Ocean Engineering, 205*, 107305. https://doi.org/10.1016/j.oceaneng.2020.107305

Yu, A., Zou, Z., Zhou, D., Zhen, Y., & Luo, X. (2020). Investigation of the correlation mechanism between cavitation rope behavior and pressure fluctuations in a hydraulic turbine. *Renewable Energy, 147*, 1199-1208. https://doi.org/10.1016/j.renene.2019.09.096

Yuan, C., Zhu, L., Liu, S., Zunling, D., & Li, H. (2022). Numerical study on the cavitating flow through poppet valves concerning the influence of flow instability on cavitation dynamics. *Journal of Mechanical Science and Technology, 36*, 761-773. https://doi.org/10.1007/s12206-022-0124-8

Zhang, G., Zhang, H. T., Wu, Z. Y., Wu X., Kim, H. D., & Lin, Z. (2024). Experimental studies of cavitation evolution through a butterfly valve at different regulation conditions. *Experiments in Fluids, 65*, 4. https://doi.org/10.1007/s00348-023-03743-3